**EMITTER International Journal of Engineering Technology**
Vol. 10, No. 1, June 2022, pp. 83~101
DOI : 10.24003/emitter.v10i1.638

# Design Analysis of Array of Dipole Transmitters for Wireless Power Transfer

**Victor O. Adewuyi[1], Milembolo J. Miantezila[2], Eunice Owoola[3]**

[1,2] School of Electronics and Information Engineering, Changchun University of Science and Technology, Changchun, 130022, China
[3] School of Electronics and Information Engineering, Hebei University of Technology, Tianjin, 300401, China
Correspondence Author : 2018300111@mails.cust.edu.cn

*Received January 10, 2022; Revised February 14, 2022; Accepted March 18, 2022*

**Abstract**

Considered in this work are the radiation aspects of a radio-frequency wireless power transfer system. Using the halfwave dipole as a candidate of choice, the current distribution on the antenna is first evaluated and presented using the versatile electromagnetic numerical Method of Moment technique (MoM). Using the current distribution obtained from the kernel of integration, the radiation fields for the single dipole element was obtained. Also, the analysis is extended to uniformly space linear antenna arrays using broadside and ordinary endfire arrays as candidates of interest. The simulation results for the broadside and endfire arrays were presented for 5, 6, 7, 10, 20 and 30 array elements at 0.3, 0.4 and 0.5 inter-element spacing. The peak directivity of broadside array occurs at 30 elements, 0.5λ spacing, and exceeds endfire array peak directivity by 11.27%. In addition to the advantage of an improved directivity achieved by the 7-element broadside array, an improved peak sidelobe level (PSLL) with the lowest PSLL for 7, 20, and 30 elements broadside array occurring at -12.0534 dB, -12.4298 dB, -12.6642 dB, -13.2246 dB, and -13.2747 dB respectively.

**Keywords**: Method of Moment, Directivity, Endfire, Broadside, Sidelobes

## 1. INTRODUCTION

Wire antennas are famous for their ubiquitous applications in communications systems, and most especially for the fundamental information it provides in understanding antenna behavior and performance. They have been used in different shapes and modifications to meet specific design needs such as directivity, gain, etc. Wireless Power Transfer systems are generally classified based on different parameters, such as strength of coupling, means of coupling, and distance of coupling. Based on coupling strength, WPT systems can be either loosely coupled WPT (LC-WPT) or strongly coupled WPT (SC-WPT); based on means of coupling, it can be magnetic resonant coupling [1], inductive coupling [2], capacitive coupling (C-

WPT) [3], or microwave; and based on distance of radiation, it can be near-field (non-radiative) or far-field (radiative) [4]. The analysis of far-field radiative transmission is considered in this work. Although WPT technology is already available commercially, most current techniques are based on the principle of near-field which limits the distance to few centimeters. The *Qi* standard for mobile phones wireless chargers for instance, restricts the distance between the charging pad and the device to 4cm [5]. The long distance possibility of Far-field transmission makes it more flexible and suitable option for power multicasting, however at a trade-off of poor transmission efficiency due to huge path loss. Approaches to reduce this include concentrating energy using laser beams or using antenna array to execute energy beamforming [6].

The study on wireless power transmission using antennas is as early as a century ago; from the description of power absorption by Reinhold Rudenberg in 1908 [7] to the practical demonstration of wireless power transmission by Nikola Tesla in 1904 [8], and his patent in 1914 where the configuration of the system was published [9]. However, despite the wide prospects of the technology [10], the progress of antenna in wireless communication has since overtaken the development of wireless power transfer (WPT) using radio waves because of the unique challenges, such as the difficulty in maintaining higher power transmission efficiency (PTE) over longer transmission distances [11]. Although far-field evanescent resonant-coupling techniques can transmit energy at distances longer than the near-field induction methods [12, 13], much research attention is focused on near-field power transmission [14, 15], whose application can be found in consumer electronics, biomedicals, electric vehicles, etc.[16-18]. This is basically due to the drastic decrease in efficiency of wireless power transfer when using radiative method. This work considers the effect of number of element of linear array of dipole antenna on the directivity for Far-field WPT application [2]. Based on the coupled mode theory, the efficiency of power transmission using two dielectric disks and capacitivelyloaded wire loops were investigated to determine the coefficient of coupling. Other methods such as multistage filter theory and conventional circuit theory have also been used to demonstrate wireless power transfer systems [19, 20]. In [11], the characterization of two types of antennas – dipole and loop antennas were conducted to investigate wireless power transmission by near-field coupling. Using dipole as the transmitting antenna, and the loop antenna as the receiving antenna, the procedure demonstrated the influence of impedance matching and ohmic losses in the wireless power transmission system. Also, a numerical method based on the Method of Moments (MoM) was used by Poon [4] to determine the efficiency between two loops using self- and mutual-admittances. It was shown that the transfer efficiency of a given loop radius is maximized at a particular frequency, and as the radius of the loop increases, the frequency decreases.

## 2. RELATED WORKS

In an earlier work, the analysis of dipoles and array of dipoles was considered [1, 5]. This work extends the analysis to application of dipole array in wireless power transfer system. Although dipoles are used in this work, the principle is applicable to other antenna types such as loop antenna, horn antenna etc. However, the dipole antenna is considered due to its simplicity, versatility and fundamental role it plays in understanding other antennas [6]. Recent Progress in WPT research is helping in the realization and development of alternative systems for powering battery-reliant devices, hence addressing the bottlenecks and issues related to the use of batteries. Some of the outstanding benefits of the WPT system include improving portability and user-friendliness of devices by eliminating wires; enhancing design flexibility as devices can now be developed without the environmental constraints as in the case of medical implantation and underwater witricity. In order to achieve a stable and functional WPT system for robots, analysis of the WPT coupling mechanism, coupling coils and compensation topology was carried out using simulations [21]. Also, other means of enhancing coupling performance were examined, this includes Multi-layer coil structure. By using circuit theory, a modelling method based on mutual inductance theory, an accurate modelling of various components of the system is obtained to solve parameters [18, 22-24]. Towards enhancing the distance and efficiency of transmission, antenna arrays have been adopted due to their efficiency in terms of high directivity, high gain, adaptive beam steering and beamforming [25-30]. The antenna directivity increases with increasing number of array elements, with higher sidelobe level as a drawback [27]. By generating narrower beamwidths, transmission loss due to sidelobes bac propagation reduces because the energy is focused at a lower collection region [29]. The design of the desired beam-width is done by several methods, including determining the excitation currents of the transmitting antennas using efficient and effective algorithms such as biogeography-based optimization [29], mayfly algorithm [27] as well as other evolution optimization algorithms [27]. Flat-topped beams were designed using Woodward Lawson method, and applied for microwave power application at volcanoes [30]. Using brain storm algorithm, the optimization of beam collection efficiency was performed with consideration of constraints such as number of array elements, aperture and minimum array spacing [26].

## 3. ORIGINALITY

In this work, an analysis on the current distribution on the single element dipole antenna is first examined, using Method of Moment, and afterwards examines the radiation directivity and sidelobe levels of broadside and endfire arrays of dipole antenna. The Method of Moment is a full-wave and rigorous numerical technique that is used for solving electromagnetic problems with open boundaries such as antenna radiation. The mathematical foundations of the MoM were introduced in 1967 by Roger Harrington in Matrix Methods for Field Problems [1]. The MoM treatment of a wire antenna involves the

determination of the current distribution on the wire, and using this to calculate the antenna's radiation characteristics and field impedances. First, the Electric field Integral Equation (EFIE) is developed from Maxwell's Integral Equations, to obtain the Pocklington EFIE or Hallen EFIE. Applying MoM to the EFIE involves .In the next section, the system equations for the current distribution on a single element dipole antenna are first presented, using MoM; as well as the radiatied fields and system radiation parameters. Next, the system equations are computed using Matlab and the results are presented and analysed where the impact of array spacing and number of antenna elements on directivity and sidelobes level are examined and on end-fire and broadside arrays.

## 4. SYSTEM DESIGN

The analytical formulation of the characteristic equations of the system starts with the determination of the current distribution on a single element dipole antenna and the determination of the radiated field.

### 4.1 Current Distribution

Consider a dipole antenna centered at the origin and running along the z-axis as shown in figure 1.

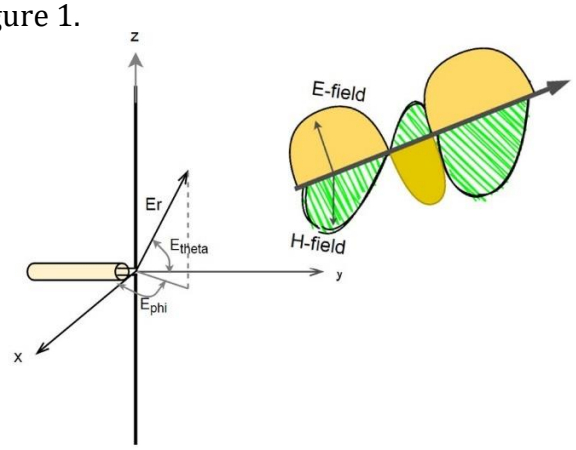


**Figure 1.** Z-polarized dipole antenna

The standing wave distribution on the wire antenna is sometimes assumed using the sinusoidal approximation, based on the assumption that the current vanishes at the end of the distribution.

$$I(z') = \hat{a}_z I_0 \, sin\left[\frac{kl}{2} - kz'\right] \text{for } -\frac{l}{2} \leq z' \leq \frac{l}{2} \quad (1)$$

Where $I(z')$ denotes the standing wave current along the z-oriented dipole antenna of length *l*. Although the sinusoidal approximation is ideal for filamentary wires, the current of wires in reality does not follow an exact sinusoidal distribution due to the non-zero radius of wire and finite gap spacing at the terminal [31]. Consider the dipole antenna given in Figure 1 as a Perfect Electric Conductor (PEC) with center excitation of 1V. This leads to the formation of a Standing Wave Voltage Ratio (VSWR) and current distribution around the geometry of the wire.

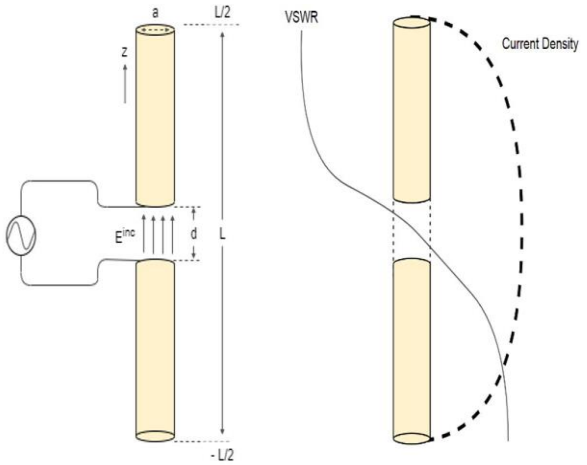


**Figure 2.** Perfect Electric Conductor Dipole fed with excitation voltage through a small air gap, d

To determine the current distribution using the method of moment, the Electric Field Integral Equation (EFIE) for the antenna is first formulated in terms of the unknown current. Starting with the point form of Maxwell's equations.

$$\nabla \times \bar{H} = \bar{J} + j\omega\varepsilon\bar{E} \tag{2}$$

$$\nabla \times \bar{E} = -j\omega\mu\bar{H} \tag{3}$$

$$\nabla \cdot \bar{B} = 0 \tag{4}$$

$$\nabla \cdot \bar{D} = \rho_v \tag{5}$$

Where $\bar{H}, \bar{E}, \bar{B}, \bar{D}$ refers to electric and magnetic field intensities, magnetic induction, electric displacement; and $\bar{\rho}, \bar{J}$ are volume charge density and electric current density. From Gauss-Maxwell's equation for the divergence of magnetic flux, the magnetic vector potential is obtained using vector identities as

$$\nabla \cdot \bar{B} = \nabla \cdot (\mu\bar{H}) = \nabla \cdot (\nabla \times \bar{A}) = 0 \tag{6}$$

The wave equation describing the electromagnetic interactions on the antenna and around the antenna is derived from the Ampere-Maxwell equation, (2),

$$\nabla \times (\nabla \times \bar{H}) = \mu\bar{J} + j\mu\omega\varepsilon\bar{E} \tag{7}$$

By vector identities of magnetic vector potential, $\bar{A}$

$$\nabla(\nabla \cdot \bar{A}) - \nabla^2\bar{A} = \mu\bar{J} + j\mu\omega\varepsilon\bar{E} \tag{8}$$

$$\nabla(\nabla \cdot \bar{A}) - \nabla^2\bar{A} - j\mu\omega\varepsilon\bar{E} = \mu\bar{J} \tag{9}$$

Where $\mu, \varepsilon$ are permittivity and permeability. From Faraday-Maxwell's equation, (2)

$$\nabla \times \bar{E} = -j\omega\mu\bar{H} = -(\nabla \times j\omega\bar{A}) \tag{10}$$

$$\nabla \times \bar{E} + (\nabla \times j\omega\bar{A}) = 0 \quad (11)$$

$$\nabla \times (\bar{E} + j\omega\bar{A}) = 0 \quad (12)$$

By vectors identities, the gradient of the scalar field ($\nabla\phi$) can be fixed as (13)

$$\bar{E} + j\omega\bar{A} = -\nabla\phi \quad (13)$$

$$\bar{E} = -(\nabla\phi + j\omega\bar{A}) \quad (14)$$

The divergence of vector potential can also be fixed to the gauge

$$\nabla \cdot \bar{A} = -j\omega\mu\varepsilon\phi \quad (15)$$

Using (14) and (15) in Equation (9),

$$\nabla^2\bar{A} - j\mu\omega\varepsilon(\nabla\phi + j\omega\bar{A}) - \nabla(\nabla \cdot \bar{A}) = -\mu\bar{J} \quad (16)$$

$$\nabla^2\bar{A} + \omega^2\mu\varepsilon\bar{A} - \nabla(j\omega\mu\varepsilon\phi\nabla \cdot \bar{A}) = -\mu\bar{J} \quad (17)$$

Applying the lorentz gauge condition, the wave equation for the electromagnetic interactions on the antenna can be presented as

$$\nabla^2\bar{A} + \omega^2\mu\varepsilon\bar{A} = -\mu\bar{J} \quad (18)$$

### a) Thin Wire Approximation (a<<L)

For the z-oriented dipole antenna presented in Figure 2, the current density is restricted to the surface of the Perfect Electric Conducting (PEC) wire, and aligned in the direction of orientation, J(0,0,z), such that (18) can be expressed as,

$$\nabla^2\bar{A}_z + \omega^2\mu\varepsilon\bar{A}_z = -\mu\bar{J}_z \quad (19)$$

Where the current density, $J_z$ and current distribution, $I(z)$ are related by

$$J_z = \frac{I(z)}{2\pi a} \quad (20)$$

### b) Far-field Approximations

At far-field, the current density decays to zero, such that

$$\nabla^2\bar{A}_z + \omega^2\mu\varepsilon\bar{A}_z = 0 \quad (21)$$

And the solution is approximated as the Green's Function, $G(z, z')$, given by,

$$G(z, z') = \frac{e^{-jkR}}{4\pi R} \quad (22)$$

To obtain the current density in the near-field of the antenna, entire volume space of the antenna is integrated using the Green's function, such that the integration kernel is zero everywhere except at the region of interest, where J ≠ 0

$$\iiint_v \mu J[G(z, z')]dv = \begin{cases} A_v (J_z \neq 0) \\ 0 \ \ (J_z = 0) \end{cases} \quad (23)$$

By substituting (20) and (22), Equation (23) can be expressed as,

$$A_z(\rho,\phi,z) = \iiint_v \mu \frac{I(z)}{2\pi a}\frac{e^{-jkR}}{R}dv \quad (24)$$

Based on the thin wire approximation, the distance R is given by,

$$R = \sqrt{(z-z')^2 + (\rho-\rho')^2} \quad (25)$$

$$R = \sqrt{(z-z')^2 + \rho^2 + a^2 - 2\rho a\, cos(\phi-\phi')} \quad (26)$$

$$\lim_{a\to 0} R = \sqrt{(z-z')^2 + \rho^2} \quad (27)$$

Hence, Equation (24) can be expressed as,

$$A_z(\rho,z) = \mu \int_{\frac{-L}{2}}^{\frac{L}{2}} I(z)\frac{e^{-jkR}}{4\pi R}dz' \quad (28)$$

### c) Enforcing the boundary Conditions ($E^{tan}$ =0)

The equivalent electric field on the dipole on Figure 3 can be expressed in terms of Equation (14), as,

$$\bar{E}_z = -(\nabla\phi + j\omega\bar{A}_z) \quad (29)$$

Substituting the Equation (15) for the static field,

$$\bar{E}_z = -\left(\nabla\left(\frac{\nabla\cdot j\bar{A}}{\omega\mu\varepsilon}\right) + j\omega\bar{A}_z\right) \quad (30)$$

$$\bar{E}_z = -\left(\frac{j}{\omega\mu\varepsilon}\frac{\partial^2\bar{A}_z}{\partial z^2} + j\omega\bar{A}_z\right) \quad (31)$$

$$\bar{E}_z = -\frac{j}{\omega\mu\varepsilon}\left(\frac{\partial^2}{\partial z^2} + \omega^2\mu\omega\varepsilon\right)\bar{A}_z \quad (32)$$

At the boundary of the PEC, the total sum of the electric fields (comprising of the scattered field, ${E_z}^{rad}$ and the incidence field,${E_z}^{inc}$) is zero;

$${E_z}^{total} = {E_z}^{inc} + {E_z}^{rad} = 0 \quad (33)$$

$${E_z}^{inc} = -{E_z}^{rad} \quad (34)$$

Where ${E_z}^{inc}$is the incident electric field striking the PEC and inducing a current density (receiving antenna); while ${E_z}^{rad}$ is the radiated electric field scattered by the applied excitation on the antenna. Applying Equations (34) and (28) on Equations (32) yields the Electric Field Integral Equation,

$${\bar{E}^{rad}}_z = \frac{j}{\omega\mu\varepsilon}\left(\frac{\partial^2}{\partial z^2} + \omega^2\mu\omega\varepsilon\right)\bar{A}_z \quad (35)$$

$${\bar{E}^{rad}}_z = \frac{j}{\omega\mu\varepsilon}\left(\frac{\partial^2}{\partial z^2} + k^2\right)\int_{\frac{-L}{2}}^{\frac{L}{2}} I(z)\frac{e^{-jkR}}{4\pi R}dz' \quad (36)$$

$$-j\omega\mu\varepsilon{\bar{E}^{rad}}_z = \left(\frac{\partial^2}{\partial z^2} + k^2\right)\int_{\frac{-L}{2}}^{\frac{L}{2}} I(z)\frac{e^{-jkR}}{4\pi R}dz' \quad (37)$$

Equation (36) is known as the Hallen's Electric Field Integral Equation; it depicts the scattered electric field at an observation point away from the antenna as a function of the unknown current distribution.

### d) MoM Treatment

To determine the unknown current using method of moment, the EFIE in (36) is related to a linear operator equation, such that the linear operator $L\{F\}$ is the RHS of (36), the response function $g$ is the unknown current distribution and the output is the applied excitation;

$$L\{F\} = g \tag{38}$$

$$L\{I(z')\} = -j\omega\varepsilon\bar{E}^{rad}{}_z \tag{39}$$

The geometry of the wire is discretized into n meshes as shown in Figure 3,

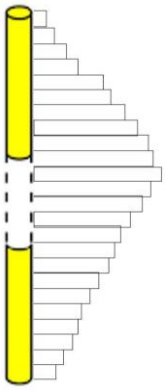

**Figure 3.** Discretization of dipole antenna geometry into N-meshes for MoM treatment

The sum of the contributions $I_n f_n(z')$ from each mesh adds up to the total current distribution, $I(z')$,

$$I(z') = I_1 f_1(z') + I_2 f_2(z') + I_3 f_3(z') + \ldots + I_N f_N(z') = \sum_{n=1}^{N} I_n f_n(z') \tag{40}$$

Expressing Equation (39) in (38),

$$L\{\sum_{n=1}^{N} I_n f_n(z')\} = -j\omega\varepsilon\bar{E}^{rad}{}_z \tag{41}$$

For effective matching, both sides are tested with a basis function, and expanded using inner product,

$$\langle v_m, L\{\sum_{n=1}^{N} I_n f_n(z')\}\rangle = \langle v_m, -j\omega\varepsilon\bar{E}^{rad}{}_z\rangle \tag{42}$$

$$\sum_{n=1}^{N} I_n \langle v_m, L\{f_n(z')\}\rangle = \langle v_m, -j\omega\varepsilon\bar{E}^{rad}{}_z\rangle \tag{43}$$

The equivalent matrix of (41) can be presented as,

$$\begin{bmatrix} \langle v_1, L\{f_1\}\rangle & \langle v_1, L\{f_2\}\rangle & & \\ \langle v_2, L\{f_1\}\rangle & \langle v_2, L\{f_2\}\rangle & & \\ & & \ddots & \\ & & & \langle v_m, L\{f_1\}\rangle \end{bmatrix} \begin{bmatrix} I_1 \\ I_2 \\ \vdots \\ I_m \end{bmatrix} = \begin{bmatrix} g_1 \\ g_2 \\ \vdots \\ g_m \end{bmatrix} \tag{44}$$

If the pulse function is used as basis function, such that

$$v_m = \begin{cases} 1(z'_{n-1} \le z' \le z'_n) \\ 0(\text{elsewhere}) \end{cases} \tag{45}$$

Such that (43) can be expanded in terms of the EFIE as,

$$\sum_{n=1}^{N} I_n \left\langle v_m, \int_{f_n} f_n(z') \left(\frac{\partial^2}{\partial z^2} + k^2\right) \frac{e^{-jkR}}{4\pi R} dz' \right\rangle = -j\omega\varepsilon\langle v_m, \bar{E}^{rad}{}_z\rangle \tag{46}$$

Equation (43) and the matrix in (44) can be related using,

$$[Z_{mn}][I_n] = [g_m] \tag{47}$$

Where the impedance matrix is given by,

$$z_{mn} = \int_{v_m} v_m \int_{f_n} f_n(z') \left(\frac{\partial^2}{\partial z^2} + k^2\right) \frac{e^{-jkR}}{4\pi R} dz' \tag{48}$$

$$g_m = -j\omega\varepsilon \int_{v_m} v_m \bar{E}^{rad}{}_z dz \tag{49}$$

$$[I_n] = [Z_{mn}]^{-1}[g_m] \tag{50}$$

The impedance matrix is computed and the current distribution, is determined. The Matlab antenna toolbox is used for the computation.

## 4.2 Radiated Fields

Expressing the E-field and H-field in terms of the magnetic vector potential [32]. Where the spherical component of the magnetic vector potential can be expressed using coordinate matrix transformation as,

$$A_z = \begin{bmatrix} A_\theta \\ A_r \\ A_z \end{bmatrix} = \begin{bmatrix} A_z \cos\theta \\ -A_z \sin\theta \\ 0 \end{bmatrix} \tag{51}$$

And

$$E_\theta = -j\omega A_\theta$$
$$H_\varphi = \frac{E_\theta}{\eta} = \frac{-j\omega A_\theta}{\eta} \tag{52}$$

Hence,

$$E_\theta = \frac{j\omega\mu}{4\pi} \int_{\frac{-l}{2}}^{\frac{l}{2}} \bar{I}(z') \frac{e^{-jkR}}{R} dz' \tag{53}$$

## 4.3 Array Design

For a uniform set of N-element antenna, the total field radiated by the antenna array is expressed as a product of the field of a singular element and the array factor. The total field radiated by an N-element uniform linear array can be expressed in a form given as,

$$E^t(\theta) = \left[[Field\ of\ a\ single\ element] \times [Array factor]\right] \tag{54}$$

While the first term is a function of the individual element, the second term is a function of the number of elements, geometrical arrangement, relative magnitudes, relative phases as well as inter-element spacings. Examples of array arrangements include as Chebychev, Broadside, Circular, etc. The array factor (AF) considered in this work is the uniform linear array, given by,

$$AF(\theta) = 1 + e^{j(kd\cos\theta+\beta)} + e^{j2(kd\cos\theta+\beta)} + \ldots + e^{j(N-1)(kd\cos\theta+\beta)} \tag{55}$$

Which can also be expressed in terms of $\psi = kd\cos\theta + \beta$, as

$$AF(\psi) = \sum_{n=1}^{N} e^{j(n-1)\psi} \tag{56}$$

And the normalized form is given by,

$$(AF)_n = \left[\frac{sin\left(\frac{N}{2}\psi\right)}{N\left(\frac{\psi}{2}\right)}\right] \tag{57}$$

Where N is the number of Array elements; k is the wave vector and d is the uniform interelement spacing. The peak sidelobe level (PSLL) of the antenna array is estimated from the Array factor and is given as [27]: $SLL = AF_n(\theta_{SL}^{SR})$

$$\text{s.t. } \theta_{PSL}^{SR} \in \max\left[0, \theta_{SR1}\right] \cup \left[\theta_{SR2}, \pi\right] \tag{58}$$

$$\theta_{PSL}^{SR} \in max[0, \theta_{SR1}] \cup [\theta_{SR1}, \pi] \tag{59}$$

Where $\theta_{SL}^{SR}$ is the PSLL angle .$[0, \theta_{SR1}]$ and $[0, \theta_{SR2}]$ are the regions of the sidelobes respectively from which the peak SLL is determined.

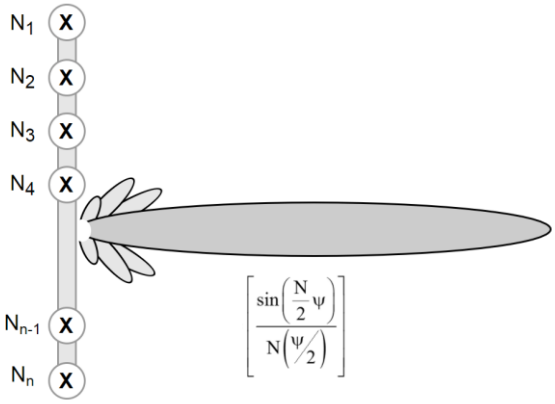


**Figure 4.** Uniform Linearly spaced Array

### a) Broadside Array

When the array design requires the maximum of the radiation pattern at broadside direction, i.e $\theta_{max}$, the broadside array design is deployed. Since,

$$\lim_{\psi \to 0} \frac{\sin \psi}{\psi} = 1 \tag{60}$$

The maximum occurs when $\psi = 0$. Hence,

$$\psi = 0 = kd\cos\theta + \beta|_{\substack{\theta=0 \\ \beta=0}} \tag{61}$$

### b) Ordinary End-fire Array

When the array design requires the maximum of the radiation pattern at $\theta_{max}$, the end-fire array design is deployed. To satisfy equation (59), the condition for maximum at $0^0$ is,

$$\psi(0) = kd + \beta = 0$$
$$\beta = -kd \tag{62}$$

And the condition for maximum at angle $180^0$ is,

$$\psi(180) = -kd + \beta = 0$$
$$\beta = kd \tag{63}$$

## 5. Results and Discussion

The results of the methods and models presented in the last section are displayed and discussed here with the help of rectangular and polar plots using Matlab. First, the current distribution and the field radiated by a single element are presented and subsequently extended to the array of 5, 6, 7 elements.

### 5.1 Current Distribution and E-field of single Element

The current distribution along the geometry of the half-wave dipole antenna as well as the elevation and azimuth plot of the electric field is presented here. In Figure 5a, the plots of the current distribution obtained using Hallen's Integral and that of the assumed sinusoidal current distribution are plotted. The moment method technique employed in this work is adapted from the electromagnetic toolbox [32]. This is presented in comparison with the general approximate sinusoidal current distribution in Figure 5a. Figures 5b and 5c present the elevation and azimuthal plane of the Electric field radiated by the dipole antenna.

From Figure 5a, it is seen that the current distribution vanishes at the ends of the wire, while it peaks at the middle of the wire and there is good agreement between the current distribution obtained numerically (MoM) and the one obtained from the sinusoidal current distribution. The arc shape of the current distribution is in agreement with the typical pattern of the standing wave on a dipole at half-wavelength [31, 33, 34], which is the efficient electrical length for transmission and the reason for which it is recommended for resonant radiative transmission. Also, the radiation pattern in Figure 5b is consistent with the expected doughnut shape with directivity of 1.5 [31].

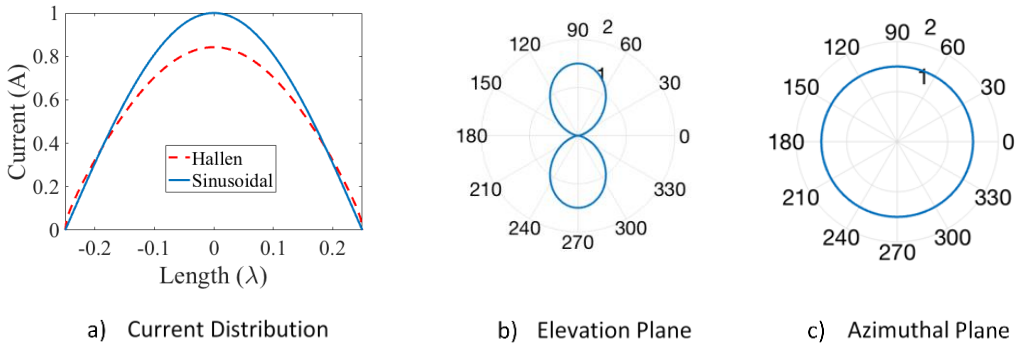


**Figure 5.** Half-wave dipole (a) Current Distribution Hallen EFIE vs Sinusoidal (b) Electric Field Elevation plane (c) Electric Field Azimuthal plane

### 5.2 Radiation Pattern of Arrays (N = 5, 6, 7 and 10, 20, 30 Elements)

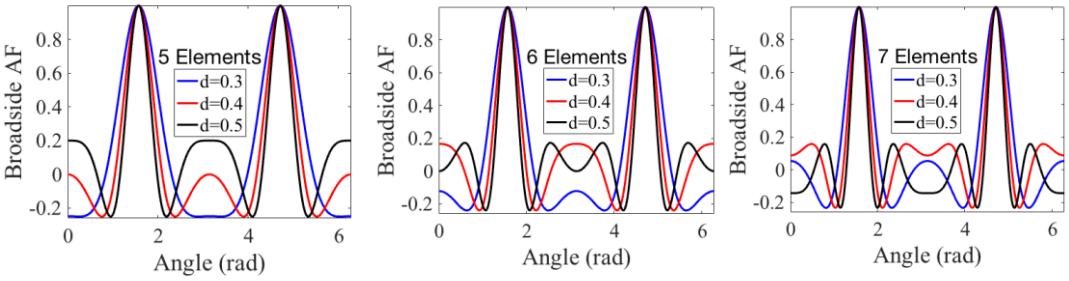


a) 5 Elements b) 6 Elements c) 7 Elements

**Figure 6.** Broadside Array of Dipole Antennas at varying inter-element distances for (a) 5 elements (b) 6 elements (c) 7 elements

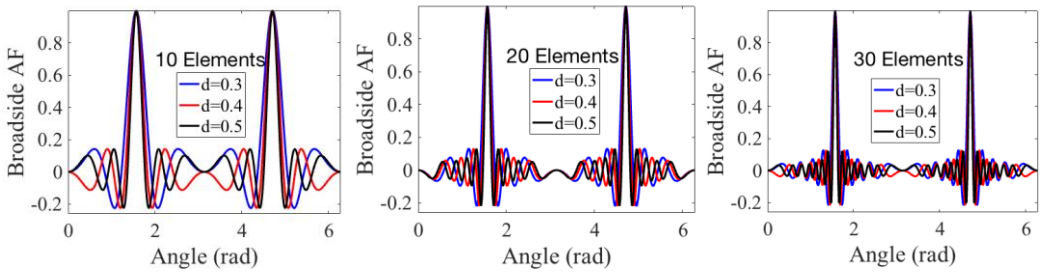


a) 10 Elements b) 20 Elements c) 30 Elements

**Figure 7.** Broadside Array of Dipole Antennas at varying inter-element distances for (a) 5 elements (b) 6 elements (c) 7 elements

As depicted in Figures 6 and 7, the radiation pattern of the broadside array, in addition to having maximums at $90^0$ and $270^0$, also have increase in directivity as the number of elements increases with a trade-off of increase in side-lobes which is consistent with expectations [31, 32]. This implies the system produces minimum sidelobes when the array element is less than 5, with a drawback of lesser directivity; and higher directivity when the array is above 30 but with a drawback of higher sidelobes. Hence, the band of the number of array elements is limited to N = 5, 6, 7 and N = 10, 20, 30 to avoid redundant duplication of existing literature [27, 34, 35]. Also, this range is sufficient in showing the potential of linear array of dipole for WPT applications, which is the scope of this investigation. At an inter-element spacing of 0.5λ, a split is experienced in the side-lobes as the number of elements is increased to 6; at 0.4λ, this initial side-lobe splitting is experienced as the number of elements is increased to 7. Figures 8 and 9 depict the radiation pattern of the endfire showing the maximums occur at $0^0$ and $180^0$ as expected [27, 34, 35]. However, an interesting disparity is observed between 0.5λ inter-element spacing and the other two considered. First, the $180^0$ main lobe does not exist for the 0.3λ and 0.4λ spacing; the mainlobe appears to be replaced by a

suppressed and splitted side-lobe. While the mainlobe for 0.5λ exists at $0^0$ and $180^0$, the projection of the unnormalized radiation pattern appears in the opposite region.

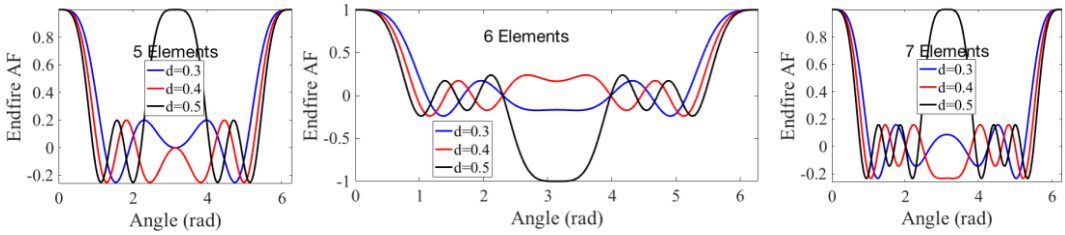


a) 5 Elements b) 6 Elements c) 7 Elements

**Figure 8**. Endfire Array of Dipole Antennas at varying inter-element distances

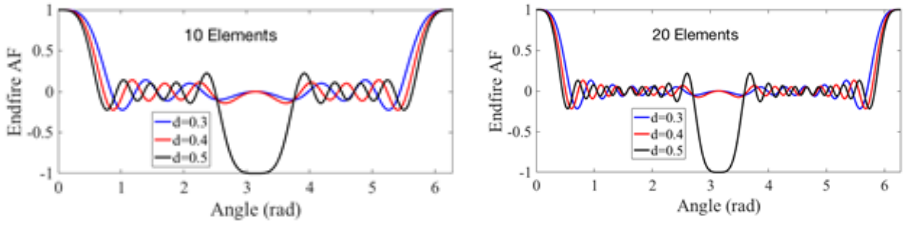


a) 10 Elements b) 20 Elements

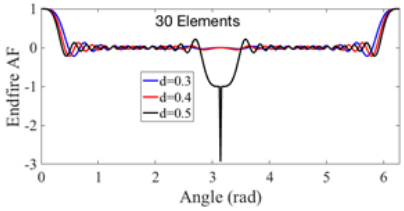


c) 30 Elements

**Figure 9**. Endfire Array of Dipole Antennas at varying inter-element distances

### 5.3 Directivity of Arrays (N = 5, 6, 7 and 10, 20, 30 Elements)

In Figures 10a, 10b, 10c and 10d, the plot of the directivity against the inter-element spacing is presented for the test number of elements for broadside and end-fire array respectively. Figures 10a and 10b shows that the directivity of the broadside array increases with increasing number of elements for both the Array Factor and total element, which is also consistent with expectation [31, 32]. The disparity between the directivity of broadside and endfire accrues to the steering of the mainlobe of endfire from the direction of the mainlobe of antenna hence resulting in split [31, 32].

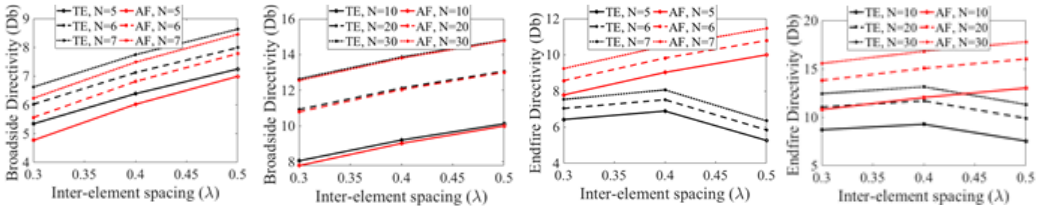


a) Broadside, N=5,6,7 b) Broadside, N=10,20,30 c) Endfire, N=5,6,7 d) Endfire, N=10,20,30

**Figure 10.** Directivity of Endfire Array for AF and Total Field

## 5.4 Sidelobe Levels

For the broadside array the lowest PSLL is achieved when the distance between each element is 0.5$\lambda$, as shown in Table 1. The lowest PSLL for 5, 6, 7, 20 and 30 elements broadside array at a uniform inter-element distance of 0.5$\lambda$ are -12.0534 dB, -12.4298 dB, -12.6642 dB, -13.2246 dB, and -13.2747 dB respectively. For 10-element, the minimum PSLL was gotten at the inter-element spacing of 0.4$\lambda$. In addition to the advantage of an improved directivity achieved by the 30 elements broadside array is also a lower PSLL. The design of 10, 16, 20 and 32 elements uniform linear broadside array at equidistance of 0.5$\lambda$ carried out by Owoola et al. gave a peak SLL of approximately -12.97 dB, -13.15 dB, -13.22 dB, and -13.25 dB, respectively [27]. Saxena & Kothari, likewise obtain the same result for 10 and 16 element broadside array [36]. This also proves that as the element number increases the peak SLL may reduce, though with an increase in the number of sidelobes. Typically, as the number of antenna elements increases, so does the directivity and gain [37]. It can be seen in Fig. 11 to Fig. 13 that the mainlobe becomes narrower as the number of elements increases, which show that the array is more directive. For the end-fire array, the lowest PSLL of -12.4317 dB, -12.6569 dB, and -13.2297 dB were obtained by 6, 7 and 30 elements respectively at the distance 0.3 $\lambda$. The 5-element, 10-element, and 20-element end-fire arrays have their lowest peak SLL at 0.5 $\lambda$ inter-element spacing. At 0.5 $\lambda$, end-fire radiation exists concurrently in the direction of $0^0$ and $180^0$ which agrees with the discovery of Balanis [31] and seen in Figs.13 and 14. Therefore, to obtain only one end-fire maximum and prevent grating lobes, the maximum inter-element spacing must be less than 0.5 $\lambda$ [31, 38, 39].

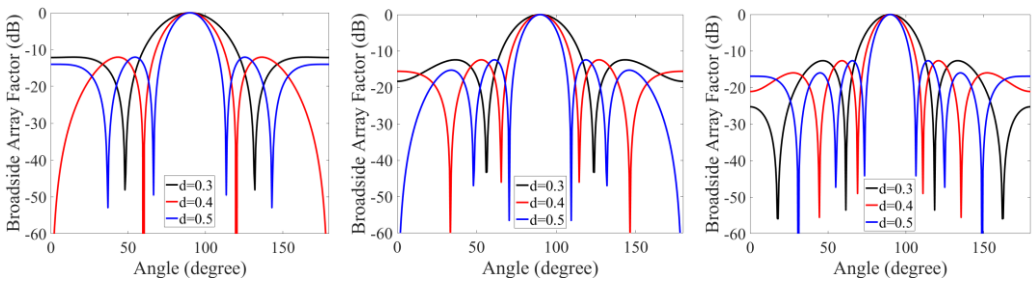


(a) 5 Elements (b) 6 Elements (c) 7 Elements

**Figure 11**: Sidelobe level of broadside Array of dipole antennas at varying inter-element distances for. (a) 5 elements (b) 6 elements (c) 7 elements

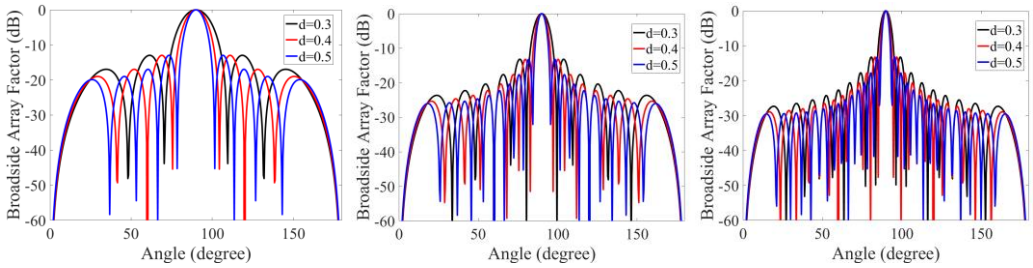


(a) 10 Elements (b) 20 Elements (c) 30 Elements

**Figure 12**: Sidelobe level of broadside Array of dipole antennas at varying inter-element distances for. (a) 10 elements (b) 20 elements (c) 30 elements

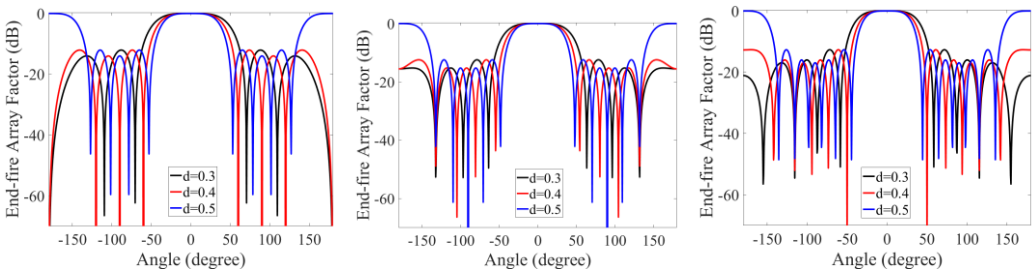


(a) 5 Elements (b) 6 Elements (c) 7 Elements

**Figure 13**: Sidelobe level of Endfire Array of dipole antennas at varying inter-element distances for. (a) 5 elements (b) 6 elements (c) 7 elements

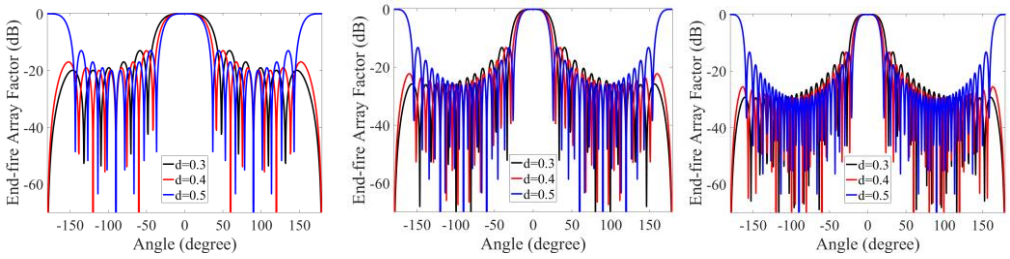


(a) 10 Elements (b) 20 Elements (c) 30 Elements

**Figure 14**: Sidelobe level of Endfire Array of dipole antennas at varying inter-element distances for. (a) 10 elements (b) 20 elements (c) 30 elements

The analysis conducted in this work shows that increasing the number of elements of the linear array will not only increase the directivity but could also improve the PSLL, depending on how the broadside or end-fire antenna array is been designed with regards to element spacing.

**Table 1:** The PSLL for the broadside and end-fire array

| Number of Elements | Broadside array PSLLs (dB) | | | End-fire array PSLLs (dB) | | |
|---|---|---|---|---|---|---|
| | 0.3 $\lambda$ | 0.4 $\lambda$ | 0.5 $\lambda$ | 0.3 $\lambda$ | 0.4 $\lambda$ | 0.5 $\lambda$ |
| 5 | -12.0414 | -12.0467 | 12.0534 | -12.0417 | -12.0414 | -12.0436 |
| 6 | -12.4275 | -12.4255 | -12.4298 | -12.4317 | -12.4256 | -12.4302 |
| 7 | -12.6551 | -12.6523 | -12.6642 | -12.6569 | -12.6524 | -12.6524 |
| 10 | -12.9691 | -12.9716 | -12.9704 | -12.9683 | -12.9679 | -12.9686 |
| 20 | -13.2052 | -13.195 | -13.2246 | -13.1882 | -13.1882 | -13.1976 |
| 30 | -13.2317 | -13.2332 | -13.2747 | -13.2297 | -13.2366 | -13.2294 |

## 6. Conclusion

Design aspects of an array of dipole antenna for radiative wireless power transfer systems have been considered in this work. Using the versatile electromagnetic MoM technique, the current distribution on the halfwave dipole was evaluated using Hallen's electric field integral equation. Towards improving the system directivity, uniform arrays of linearly spaced dipole antenna was also presented for the endfire and broadside array. The simulation figures were presented, and a comparative analysis between broadside and endfire arrays was conducted using radiation pattern, directivity and sidelobe levels as the figure of merits. From the results obtained for the scope of investigation, the peak directivity of 14.81 dB occurs on broadside array at 30 element, 0.5λ spacing and PSLLs of -13.2747 dB, while the peak directivity of 13.1425 occurs for endfire array at 30element, 0.4λ and -13.2297 dB. In addition to the advantage of an improved directivity achieved by the 7-element broadside array, an improved peak sidelobe level (PSLL) with the lowest PSLL for 7, 20, and 30 elements broadside array occurring at -12.0534 dB, -12.4298 dB, -12.6642 dB, -13.2246 dB, and -13.2747 dB respectively. The peak directivity of broadside array occurs at 30 elements, 0.5λ spacing, and exceeds endfire array peak directivity by 11.27%, hence recommended for use in WPT application. Further studies would be channelled towards techniques for improving power transfer efficiency, such as pattern synthesis; and the design of optimal simultaneous wireless information and power transfer (SWIPT).

## Acknowledgements

We would like to acknowledge the support of the Optic Fibre Research Team, Electronic Science and Technology Department, Changchun University of Science and Technology and Petroleum Technology Development Fund.

## REFERENCES

[1] V. Adewuyi, J. Milembolo, M. Munochiveyi, and E. Owoola, **Characterization of Compensation Topologies for Wireless Power**

**Transfer System**, in *2021 International Conference on Electrical, Computer, Communications and Mechatronics Engineering (ICECCME)*, 2021, pp. 1-6: IEEE.

[2] A. Kurs, A. Karalis, R. Moffatt, J. D. Joannopoulos, P. Fisher, and M. J. s. Soljačić, **Wireless power transfer via strongly coupled magnetic resonances**, vol. 317, no. 5834, pp. 83-86, 2007.

[3] M. Kline, I. Izyumin, B. Boser, and S. Sanders, **Capacitive power transfer for contactless charging**, in *2011 Twenty-Sixth Annual IEEE Applied Power Electronics Conference and Exposition (APEC)*, 2011, pp. 1398-1404: IEEE.

[4] A. S. J. P. I. E. R. Poon, **A general solution to wireless power transfer between two circular loop**, vol. 148, pp. 171-182, 2014.

[5] M. Xia and S. J. I. t. o. s. p. Aissa, **On the efficiency of far-field wireless power transfer**, vol. 63, no. 11, pp. 2835-2847, 2015.

[6] J. Huang, Y. Zhou, Z. Ning, and H. J. I. w. c. Gharavi, **Wireless power transfer and energy harvesting: Current status and future prospects**, vol. 26, no. 4, pp. 163-169, 2019.

[7] R.-F. Xue, K.-W. Cheng, M. J. I. T. o. C. Je, and S. I. R. Papers, **High-efficiency wireless power transfer for biomedical implants by optimal resonant load transformation**, vol. 60, no. 4, pp. 867-874, 2012.

[8] N. J. E. W. Tesla and Engineer, **The transmission of electrical energy without wires**, pp. 429-431, 1904.

[9] M. Schmorrow and D. Schmorrow, **Innovation Lessons: Implications of Nikola Tesla's Life for Today's Engineers, Scientists, and Technology Designers**, in *International Conference on Human-Computer Interaction*, 2015, pp. 183-186: Springer.

[10] J. O. McSpadden and J. C. J. I. m. m. Mankins, **Space solar power programs and microwave wireless power transmission technology**, vol. 3, no. 4, pp. 46-57, 2002.

[11] Q. Chen, K. Ozawa, Q. Yuan, K. J. I. A. Sawaya, and P. Magazine, **Antenna characterization for wireless power-transmission system using near-field coupling**, vol. 54, no. 4, pp. 108-116, 2012.

[12] J. Murakami *et al.*, **Consideration on cordless power station-contactless power transmission system**, vol. 32, no. 5, pp. 5037-5039, 1996.

[13] K. Hatanaka *et al.*, **Power transmission of a desk with a cord-free power supply**, vol. 38, no. 5, pp. 3329-3331, 2002.

[14] D. Patil, M. K. Mcdonough, J. M. Miller, B. Fahimi, and P. T. J. I. T. o. T. E. Balsara, **Wireless power transfer for vehicular applications: Overview and challenges**, vol. 4, no. 1, pp. 3-37, 2017.

[15] S. Jayalath, A. J. I. J. o. E. Khan, and S. T. i. P. Electronics, **Design, Challenges, and Trends of Inductive Power Transfer Couplers for Electric Vehicles: A Review**, 2020.

[16] M. J. Schormans, **Inductive Links for Biomedical Wireless Power and Data Telemetry: Circuits and Methods**, UCL (University College London), 2019.
[17] M. Schormans, V. Valente, A. J. I. T. o. B. C. Demosthenous, and Systems, **Practical inductive link design for biomedical wireless power transfer: A tutorial**, vol. 12, no. 5, pp. 1112-1130, 2018.
[18] B. Lee, M. Kiani, M. J. I. t. o. b. c. Ghovanloo, and systems, **A triple-loop inductive power transmission system for biomedical applications**, vol. 10, no. 1, pp. 138-148, 2015.
[19] Y. Tak, J. Park, S. J. I. A. Nam, and W. P. Letters, **Mode-based analysis of resonant characteristics for near-field coupled small antennas**, vol. 8, pp. 1238-1241, 2009.
[20] T. Ishizaki, T. Komori, T. Ishida, and I. J. I. E. E. Awai, **Comparative study of coil resonators for wireless power transfer system in terms of transfer loss**, vol. 7, no. 11, pp. 785-790, 2010.
[21] J. Wang, M. Hu, C. Cai, Z. Lin, L. Li, and Z. J. A. A. Fang, **Optimization design of wireless charging system for autonomous robots based on magnetic resonance coupling**, vol. 8, no. 5, p. 055004, 2018.
[22] J. A. A. A. Triviño-Cabrera, **Emerging Capabilities and Applications of Wireless Power Transfer**, presented at the IGI Global, 2018.
[23] A. Kumar, S. Mirabbasi, and M. Chiao, **Resonance-based wireless power delivery for implantable devices**, in *2009 IEEE Biomedical Circuits and Systems Conference*, 2009, pp. 25-28: IEEE.
[24] M. Kiani and M. Ghovanloo, **Pulse delay modulation (PDM) a new wideband data transmission method to implantable medical devices in presence of a power link**, in *2012 IEEE Biomedical Circuits and Systems Conference (BioCAS)*, 2012, pp. 256-259: IEEE.
[25] Y.-F. Cheng, X. Ding, W. Shao, and C. J. I. A. Liao, **A high-gain sparse phased array with wide-angle scanning performance and low sidelobe levels**, vol. 7, pp. 31151-31158, 2019.
[26] G. X. Liu, Q. Qin, Q. H. J. I. J. o. A. Zhang, and Propagation, **Linear Array Synthesis for Wireless Power Transmission Based on Brain Storm Optimization Algorithm**, vol. 2021, 2021.
[27] E. O. Owoola, K. Xia, T. Wang, A. Umar, and R. G. J. I. A. Akindele, **Pattern Synthesis of Uniform and Sparse Linear Antenna Array Using Mayfly Algorithm**, 2021.
[28] S. U. Rahman, Q. Cao, M. M. Ahmed, H. J. J. o. M. Khalil, Optoelectronics, and E. Applications, **Analysis of linear antenna array for minimum side lobe level, half power beamwidth, and nulls control using PSO**, vol. 16, pp. 577-591, 2017.
[29] G. Sun *et al.*, **Power-pattern synthesis for energy beamforming in wireless power transmission**, vol. 30, no. 7, pp. 2327-2342, 2018.
[30] N. Takabayashi, N. Shinohara, and T. Fujiwara, **Array pattern synthesis of flat-topped beam for microwave power transfer system at**

**volcanoes**, in *2018 IEEE Wireless Power Transfer Conference (WPTC)*, 2018, pp. 1-4: IEEE.
[31] C. A. Balanis, **Antenna theory: analysis and design**. John wiley & sons, 2015.
[32] S. J. Orfanidis, **Electromagnetic waves and antennas**, 2002.
[33] S. Adekola and V. Adewuyi, **On the electromagnetic characteristics of dipole antennas at MF/HF/VHF/UHF**, in *2017 IEEE 3rd International Conference on Electro-Technology for National Development (NIGERCON)*, 2017, pp. 76-85: IEEE.
[34] V. Adewuyi, T. Erinosho, and S. Adekola, **Characteristics of a single element dipole and array of dipoles at frequencies of selected TV stations in Nigeria**, in *2017 IEEE 3rd International Conference on Electro-Technology for National Development (NIGERCON)*, 2017, pp. 289-299: IEEE.
[35] K. P. J. I. J. o. A. E. R. Dutta and Science, **Study of Broadside Linear Array Antenna with Different Spacing and Number of Elements**, vol. 4, no. 5, p. 237181, 2017.
[36] P. Saxena, A. J. I. J. o. A. Kothari, and Propagation, **Optimal pattern synthesis of linear antenna array using grey wolf optimization algorithm**, vol. 2016, 2016.
[37] D. L. B. Ninu Sathianathan and J. G. , **Design and Analysis of Symmetric and Asymmetric Staircase Patch Antenna**, *IOSR Journal of Electronics and Communication Engineering (IOSR-JECE),* pp. 72-78, 2017.
[38] Y. Huang, **Antennas: from theory to practice**. John Wiley & Sons, 2021.
[39] H. Gangadhar, **Radiation Pattern for Broad Side Array and End Fire Array Antennas**, *International Journal of New Technologies in Science and Engineering,* vol. 5(5), pp. 97–105., 2018.